Research Article | Vol. 10, No. 7 | 1 Jul 2019 | BIOMEDICAL OPTICS EXPRESS 3591
Biomedical Optics EXPRESS

Five-dimensional two-photon volumetric microscopy of in-vivo dynamic activities using liquid lens remote focusing

KAYVAN FOROUHESH TEHRANI,[1] CHARLES V. LATCHOUMANE,[1] W. MICHAEL SOUTHERN,[2,4] EMILY G. PENDLETON,[1] ANA MASLESA,[1] LOHITASH KARUMBAIAH,[1] JARROD A. CALL,[1,2] AND LUKE J. MORTENSEN,[1,3,*]

[1]*Regenerative Bioscience Center, Rhodes Center for ADS, University of Georgia, Athens, GA 30602, USA*
[2]*Department of Kinesiology, University of Georgia, Athens, GA 30602, USA*
[3]*School of Chemical, Materials and Biomedical Engineering, University of Georgia, Athens, GA 30602, USA*
[4]*Currently with: Department of Biochemistry, Molecular Biology, and Biophysics, University of Minnesota, Minneapolis, MN 55455, USA*
[*]*luke.mortensen@uga.edu*

Abstract:. Multi-photon scanning microscopy provides a robust tool for optical sectioning, which can be used to capture fast biological events such as blood flow, mitochondrial activity, and neuronal action potentials. For many studies, it is important to visualize several different focal planes at a rate akin to the biological event frequency. Typically, a microscope is equipped with mechanical elements to move either the sample or the objective lens to capture volumetric information, but these strategies are limited due to their slow speeds or inertial artifacts. To overcome this problem, remote focusing methods have been developed to shift the focal plane axially without physical movement of the sample or the microscope. Among these methods is liquid lens technology, which adjusts the focus of the lens by changing the wettability of the liquid and hence its curvature. Liquid lenses are inexpensive active optical elements that have the potential for fast multi-photon volumetric imaging, hence a promising and accessible approach for the study of biological systems with complex dynamics. Although remote focusing using liquid lens technology can be used for volumetric point scanning multi-photon microscopy, optical aberrations and the effects of high energy laser pulses have been concerns in its implementation. In this paper, we characterize a liquid lens and validate its use in relevant biological applications. We measured optical aberrations that are caused by the liquid lens, and calculated its response time, defocus hysteresis, and thermal response to a pulsed laser. We applied this method of remote focusing for imaging and measurement of multiple in-vivo specimens, including mesenchymal stem cell dynamics, mouse tibialis anterior muscle mitochondrial electrical potential fluctuations, and mouse brain neural activity. Our system produces 5 dimensional (x,y,z,λ,t) data sets at the speed of 4.2 volumes per second over volumes as large as 160 x 160 x 35 μm^3.

1. Introduction

Multi-photon microscopy enables high resolution imaging and intrinsic optical sectioning at depth due to use of near-infrared and infrared laser multi-photon excitation processes. This has enabled critical insights into real-time biological function of neural networks in the brain; cell trafficking and microenvironment properties in the bone marrow; and regenerative processes in many tissues. The size scale of these biological efforts dictates tradeoffs between scan speed, resolution, and field of view. When studying events such as cell adhesion,

#361055 https://doi.org/10.1364/BOE.10.003591
Journal © 2019 Received 5 Mar 2019; revised 29 May 2019; accepted 4 Jun 2019; published 26 Jun 2019

Biomedical Optics EXPRESS

vascular flow patterns, or homing, rapid scanning of a relatively small volume is needed. In addition, for phenomenon such as neural firing, multiple events occur at different depths of the volume under study that need to be rapidly accessed [1,2]. In all of these situations, rapid lateral and axial scanning are needed to accurately capture biological dynamics. Lateral scanning that couples a galvo-driven slow axis with a fast axis using a resonant galvo or polygonal mirror can create a 2D scan field at 30-120 Hz or more depending on the field of view. Rapid axial scanning can reproducibly and precisely translate that to several volumes per second depending on the number of Z positions required.

Many point scanning microscopes generate an axial stack using mechanical displacement of the sample with a stepper motor [3], which are very precise and have several millimeters of travel, but are too slow for some live imaging applications. To rapidly scan during imaging, the objective or stage can be moved using a piezo mount, which works at several tens of hertz, but is limited by inertial forces that cause instability at higher speeds due to the weight of the objective lens. Another limitation of mechanical scanning is the addition of depth-dependent optical aberrations, especially spherical aberrations [4]. Optical strategies that use simultaneous multi-focal imaging are also possible [5–8], but require highly specialized optical setups and often have optical performance trade-offs. Remote focusing is one of the simplest methods of rapidly modulating the focal plane using an active element remotely from the sample to adjust the axial focal plane. A number of technologies and active elements to use this process in point-scanning microscopy have been proposed [9], such as a voice coil motor [10], an acousto-optic modulator [11], a TAG lens [12], a deformable mirror [13,14], a thermal lens [15], an Alvarez lens [16], and a liquid lens [17–23]. Liquid lens technology is an inexpensive and stable remote focusing technology, and uses either hydraulic pressure [20–22] or the electrowetting phenomenon [17–19] to change the optical power of the lens. Liquid lens remote focusing is an easy to implement and affordable method for fast inertia-free volumetric imaging. However, high energy pulses required for multi-photon microscopy have drawn some concerns about long term use of liquid lenses with ultrafast lasers. In addition, adoption has been slow due to perceived challenges arising from suspected optical aberrations and difficult calibration of the liquid lens.

In this work we use an electrowetting liquid lens for remote focusing in multi-photon microscopy. Electrowetting occurs at the boundary of two immiscible liquids with different refractive indices that form an electrically adjustable curvature and hence an adjustable focusing power [17], with a settling time of a few milliseconds - a timescale useful for many biological phenomena. We measured the aberrations using a Shack-Hartmann wavefront sensor (SHWFS), and characterized hysteresis of defocus and several Zernike modes of the lens using a ramp signal with different input frequencies. We further measure the step response of the liquid lens. We calibrated our system using a test target made of fluorescent beads in a gel compared with mechanical Z-scanning, and were able to rapidly and reproducibly scan volumes. These measurements and analyses enabled us to measure and characterize the wavefront, in response to the input voltage. After the calibration step, we applied this method to multi-color volumetric imaging of live cells, blood flow in the skull of a live mouse, mouse tibialis anterior (TA) muscles, and neural activity in the mouse cerebral cortex.

2. Methods

2.1. Optical setup

Our microscope (Fig. 1) uses a Ti:Sapphire laser (Coherent Chameleon Ultra II) with a wavelength range of 680nm – 1080nm, and intensity modulation using a Pockels cell (Conoptics). A second femtosecond fiber laser (Calmar Cazadero) source was used for testing the thermal reponse of the lens. The fiber laser source produces 1550 nm, 370 fs pulses which were frequency doubled to produce 775 nm. A pinhole was used at the focus of our beam expansion telescope to improve the uniformity and Gaussian properties of the beam. We

Biomedical Optics EXPRESS

limited the beam size to 2mm using an iris, which is smaller than the effective area of the liquid lens (3.9 mm) in order to minimize aberrations due to surface curvature. The liquid lens (Varioptic Arctic-39N1) was placed at a conjugate plane back pupil plane using a kinematic mount (Thorlabs KC1) to align the tip/tilt of the lens. This liquid lens uses immiscible media with the same densities, therefore it can be placed in any orientation. We used the image plane generated by L_3 as a metric for defocus using photodiodes $PD_{1,2}$ (Thorlabs FDS100). PD_1 has a pinhole in front of it to make its signal proportional to the effective focal length of the system, which is normalized by the total intensity captured by PD_2. After the liquid lens, we re-magnify the 2mm beam to use the full NA of the system using lenses L_3 and L_2.

A flip mirror diverts the optical path to a SHWFS made using a 150 µm pitch microlens array (Thorlabs MLA150-5C-M), an achromatic doublet pair (Thorlabs MAP105050-B), and a CCD camera (The Imaging Source DMK 33UP1300) capable of imaging at 500 frames per second to measure the wavefront produced by the liquid lens. The microscope path then includes a resonant-galvanometer (fast axis – slow axis) scanner (Sutter instruments MDR-R), a 60x Olympus (LUMFLN60x) water immersion objective with NA of 1.1, three photon multiplier tubes (PMTs) from Hamamatsu (H10770-40), transimpedance amplifiers (Edmund Optics 59-178), and appropriate filters and dichroic mirrors for simultaneous 3 color imaging. A National Instruments DAQ card and FPGA module were used for control and synchronization of the system, and digitizing of the amplified signal. The MATLAB-based open-source software, Scanimage [3], was employed to control the microscope. For mechanical scanning we use an X-Y-Z stage from Sutter Instruments (MPC-200).

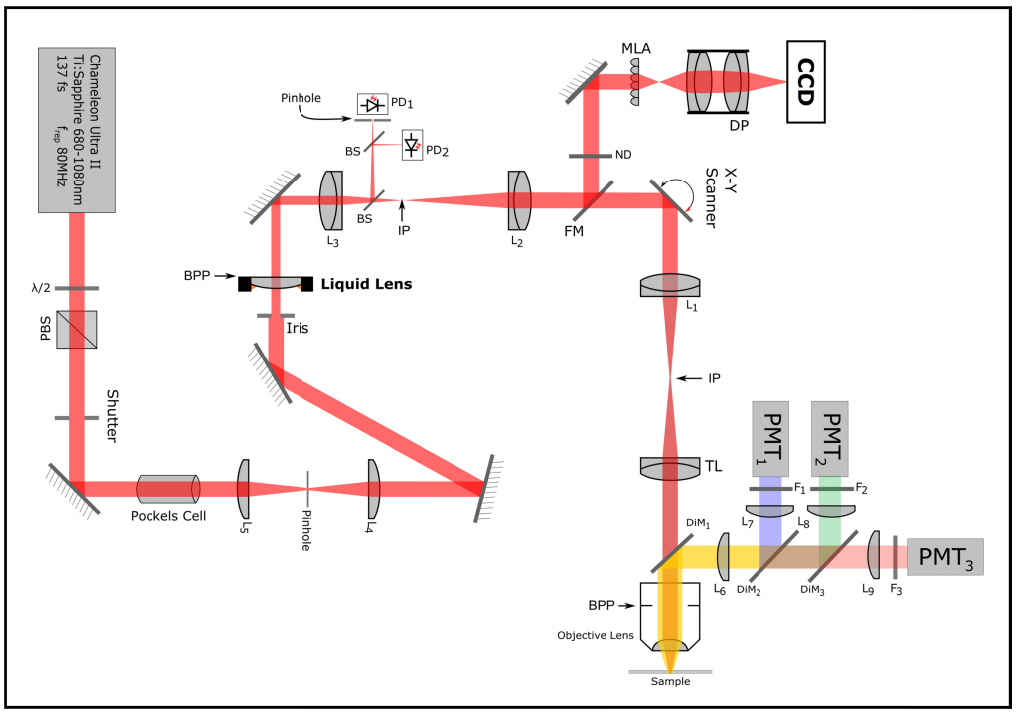

Fig. 1. - Diagram of the microscope. BS and PBS are regular and polarizing beam splitters. BPP is the back pupil plane and IP is the image plane. L is lens, DP is achromatic doublet pair, TL is tube lens, MLA is microlens array, F is filter, DiM is dichroic mirror, FM is flip mirror, ND is neutral density filter, PD is photodiode, CCD is charge coupled device camera, and PMT is photon multiplier tube.

The liquid lens has optical power range from –5 diopter to + 15 diopter. The full axial scanning range can be calculated by geometrical optics using [24,25]:

Biomedical Optics EXPRESS

$$\Delta z = \frac{1}{M^2}\frac{f_{L3}^2}{f_{LL}}n, \tag{1}$$

where M is the magnification from the sample plane to the image plane right after the liquid lens, n is the refractive index of the immersion medium, f_{L3} and f_{LL} are the focal lengths of lens L_2 and the liquid lens respectively. We calculate a theoretical 36.8 μm total focal length displacement given the optical power range of the liquid lens. This range was selected to match the 2D scanning rate of our system (110 frames per second) to provide a continuously scanned volume for a reasonable number of volumes per second (4.2 volumes/s, 26 frames per volume) for our biological imaging targets with Nyquist sampling. For other applications such as brain neural activity measurement in multiple cortical layers, this range could be altered to be as large as ~100 μm by changing the focal length of L_3 and magnification of the system to provide appropriate axial scanning.

2.2. Preparation of the fluorescent beads in a polyacrylamide gel

To produce a volume of point sources fixed in space we made a poly-acrylamide gel mixed with 200 nm fluorescent Tetraspec beads (Invitrogen T7280). The gel was made by combining 45 μl Tetraspec beads (diluted 1:50 in ultrapure water), 45 μl 30% Acrylamide (Bio-rad 1610156), 2 μl Ammonium persulfate, and 0.2 μl TEMED. The mixture was transferred to the well of a coverglass-bottom petri dish and imaged after the gel solidified.

2.3. Preparation of the cell sample

Mesenchymal stem cells (MSCs), isolated from a wild-type mouse, were grown on a 35mm Petri dish in growth medium (α-MEM, 10% fetal bovine serum, Penicillin Streptomycin, L-glutamine). MSCs were stained with lipophilic membrane dye DiD according to the manufacturer's protocol (Invitrogen) 30-40 minutes before imaging. Cells were transferred to a hemocytometer and imaged in suspension, with a heating strip and an infrared thermometer to maintain the temperature of the cells at 37° C.

2.4. Preparation of the tibialis anterior sample

The tibialis anterior (TA) muscle was extracted from a transgenic mouse with C57Bl/6 background ubiquitously expressing mitochondrial Dendra2 green/red photoswitchable monomeric fluorescent protein (Jackson Laboratory, #018385) [26], 1 hour before imaging. We permeabilized the muscle in buffer 1 containing (7.23 mM K_2EGTA, 2.77 mM CaK_2EGTA, 20 mM imidazole, 20 mM taurine, 5.7 mM ATP, 14.3 mM PCr, 6.56 mM $MgCl_2$-$6H_2O$, 50 mM MES, 100 μg/ml Saponin) for 30 minutes at 4° C. The muscle was then incubated with 50 nM TMRE in a buffer 2 (105 mM MES, 30 mM KCl, 10 mM KH_2PO_4, 5 mM $MgCl_2$- $6H_2O$, 0.5 mg/mL BSA, 0.5 M EGTA), for 15 minutes at 4° C. At the same time one drop of NucBlue (life technologies - R37606) dye was also added to the buffer to stain the nuclei. Following incubation with TMRE and NucBlue, the TA was rinsed in buffer 2 for 15 minutes. The TA was then removed and fixed to a dissection-gel petri dish at proximal and distal tendons. For imaging, the TA was submerged in buffer 2 and the following substrates were added to stimulate mitochondrial respiration: glutamate (10 mM), malate (5 mM), ADP (2.5 mM). To increase the rate of fluctuations, FCCP (1μM) was added.

2.5. Intravital imaging

For skull imaging, one hour before surgery a dose of Meloxicam (1mg/kg) was injected subcutaneously to the mouse. The mouse was initially anesthetized using 4% isoflurane (100 ml/min oxygen flow), and restrained using a 3D printed stereotaxic holder. The rate of isoflurane was then reduced to 1.5% during imaging. A 20 μL dose of 70 kDa rhodamine-B dextran (Nanocs) was administered through retro-orbital injection, to visualize the vasculature. Five minutes before making an incision, 50 μL of 0.25% bupivacaine was locally

Biomedical Optics EXPRESS

applied as analgesia. An incision was made on the scalp from between the eyes toward both the ears to make a flap. The periosteum layer was removed, and the area of imaging was cleaned using a cotton swab; immediately sterile phosphate buffered saline (PBS) was applied to the incision site. The animal was placed under the microscope objective and sterile PBS was added to fill the gap between the skull and the objective lens. After the imaging session, the animal was euthanized using CO_2 and cervical dislocation.

For mouse neural activity experiments, four weeks prior to imaging, the mouse was transduced with a viral construct encoding the red fluorescent calcium sensor jRGECO in neurons, via direct cortical injection through a cranial window that was surgically placed above the barrel cortex (3mm diameter, 120um thickness). First, the animal was anesthetized using isoflurane (4% induction and 1.6% maintained). A craniotomy was performed above the barrel cortex (AP: −2, ML: −5 from bregma), and a 1 µl dose of pAAV.Syn.NES-jRGECO1a.WPRE.SV40 [27] virus was injected (addgene: #100854; Titer: 4.1 x 10^{13} genome copies/mL), at a rate of 0.2 µl/min using a glass micropipette (Eppendorf Celltram Oil pump). A coverslip glass was positioned and cemented (UV cured dental cement, Henry Schein) on top of the craniotomy after infusion of 1% agarose on the surface of the exposed dura. Before imaging, the animal received one dose of a cocktail of ketamine/xylazine (156.25 mg/kg ketamine, 6.25 mg/kg xylazine) as anesthesia and placed on a 3D printed stereotaxic holder. Air blow stimulation were given through a PVC tube oriented towards the contralateral whiskers to the craniotomy.

All animal procedures and experiments were approved by the UGA Institutional Animal Care and Use Committee (IACUC).

3. Characterization of the liquid lens

3.1. Characterization of the liquid lens

We performed wavefront measurement to specifically characterize the optical aberrations produced by the liquid lens. For this purpose the liquid lens was directly conjugated to the SHWFS without passing through the rest of the system to eliminate system aberration contributions to the measurement. The acquired wavefronts from the SHWFS were reconstructed using the methods described in [28]. For conversion of the extracted defocus term to optical power in diopter unit we use the following formalities. The defocus term in radial coordinates has the following form [29]:

$$z(r,\theta) = c_3\sqrt{3}\left(2r^2-1\right) \tag{2}$$

where c_3 is the coefficient of the Zernike mode. We can write a general term for the focal distance f of a spherical surface [30] (Fig. 2):

$$f = z + \frac{r\left(1-\tan^2\alpha\right)}{2\tan\alpha} \tag{3}$$

$$\tan\alpha = \frac{dz}{dr} = 4c\sqrt{3}r \tag{4}$$

where α is the angle between the incident light and the perpendicular line from the center of the curvature. Combining 3 and 4 we get

$$f = c\sqrt{3}\left(2r^2-1\right) + \frac{r\left(1-\left(4c\sqrt{3}r\right)^2\right)}{2\left(4c\sqrt{3}r\right)}. \tag{5}$$

Biomedical Optics EXPRESS

Because the DC term does not contribute to the focal length we remove it from (5) and simplify it to

$$f = \frac{1}{8c\sqrt{3}}, \tag{6}$$

and therefore

$$D = \frac{1}{f} = 8c\sqrt{3}. \tag{7}$$

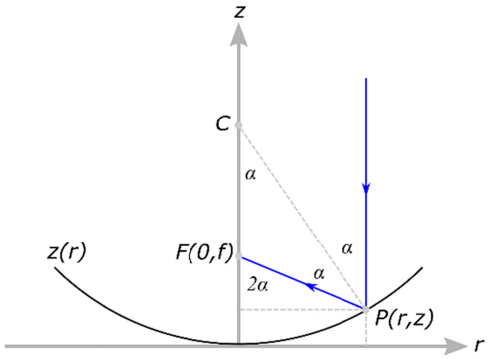

Fig. 2. - Illustration of the derivation of the defocus term.

We applied a range of voltages with a triangle waveform at frequencies of 1, 2, and 5 Hz to the liquid lens and measured the wavefront at the speed of 500 frames per second. In Fig. 3(a)-(c) we show the raw data of all the aberrations as the voltage increases and then decreases. This measurement shows that other than the defocus term, the only significant aberration is astigmatism (absolute magnitude of ~0.05 radians), and other aberrations are negligible (<0.01 rad). These measurements were performed more than 5 times, and due to consistent results, a representative measurement is shown. We then measured the hysteresis of defocus (Fig. 3(d)). We applied a square wave to measure the step response of the lens (Fig. 3(e)), with a second order fit to calculate the settling time. The step response of an undamped second order low pass system has the following form [31]

$$y(t) = A\left(1 - \frac{1}{\sqrt{1-\zeta^2}} e^{-\zeta\omega_0 t} \sin\left(\omega_0\sqrt{1-\zeta^2}\,t + \cos^{-1}\zeta\right)\right), \tag{8}$$

where A is a scaling factor, ζ is the damping ratio, and ω_0 is the natural frequency. We calculate a settling time (5 time-constants) of $t_s = 5/(\zeta\omega_0) = 92ms$ from the step response measurement and fit. Our hysteresis analysis shows that with a triangle waveform up to 5 Hz the liquid lens follows the input voltage diligently. Although the measured settling time could be a limiting factor for this specific lens when using a step function to move between focal planes, by using a triangular waveform we avoid this limitation and remain in the linear hysteresis-free region of the liquid lens. Although more rapid settling times have been achieved previously with other liquid lenses [23], the current technology in our implementation yields an axial scanning rate that is limited by the lateral scan speed of our 8 kHz resonant scanner rather than the settling time of the liquid lens. We used an Arduino circuit to create a frequency divider and convert the clock pulses from Scanimage to an analog voltage. To avoid stepping of the digitized output, we used an analog low pass filter with a cut-off frequency of 8 Hz to make a linear triangular form, without any distortion due

Biomedical Optics EXPRESS

to the settling time. Because the frequency of the triangle signal is about 2Hz for 4 volumes/second imaging, and the frequency of the digitization noise is at more than 100 Hz our input signal is smoothed without any major effect on the hysteresis.

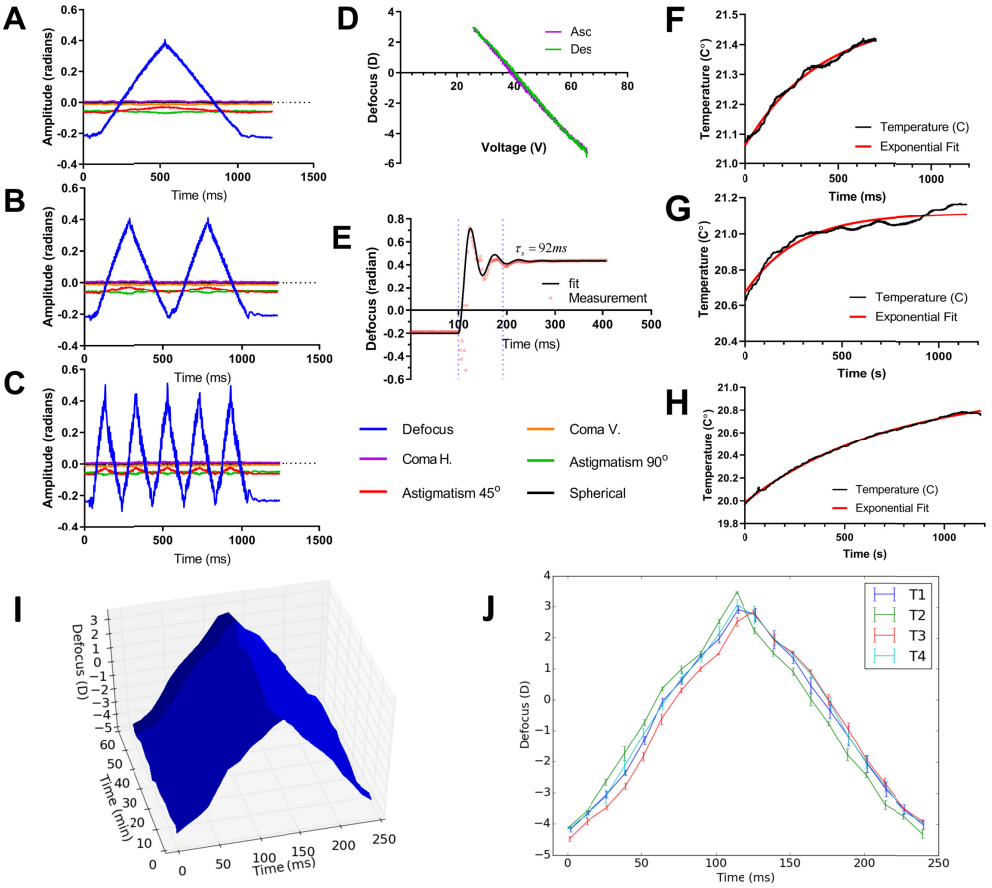

Fig. 3. Characterization of the liquid lens. A-C show wavefront measurements with triangle input waveform produced with 1, 2, and 5 Hz frequencies, respectively. D shows the hysteresis curve of the defocus terms (Asc and Des show ascending and descending hysteresis behaviors respectively). E is the step response of the defocus produced by the liquid lens, and a fit applied to it to calculate the settling time. F-H show the thermal response of the lens in response to different 54 kW, 27 kW, and 9 kW peak pulse power, respectively. I shows long term measurement of the wavefront when the liquid lens was exposed to a 100mW 775nm beam, measured at 5 minute intervals. Average of every 15 minutes (T1-T4) and the corresponding errors are shown in J.

A concern for using pulsed laser with high peak energy is the potential for thermal accumulation in the liquid lens. To test this effect, we used a fiber laser source with adjustable repetition rate and hence differing peak energy, and measured the temperature of the body of the lens. We performed the tests for 30 MHz, 10 MHz, and 5 MHz repetition rates, with constant input power of 100 mW to produce 3.3 nJ, 10 nJ, and 20 nJ pulse energy levels or 9 kW, 27 kW, and 54 kW peak pulse power respectively. We observed minimal increase in the temperature of the lens body for all tested peak powers (Fig. 3(f)-(h)). According to the manufacturer of the lens temperatures below 60°C are suitable for operation of the lens. We also measured the long term effect of the high energy pulses on the liquid lens. A 100 mW laser (Ti:Sapphire 775 nm 80 MHz) was shone on the liquid lens for a period of 60 minutes, and the wavefront was measured at intervals of 5 minutes (Fig. 3(i),(j)). The results show no

Biomedical Optics EXPRESS

significant difference, for instance the point with defocus diopter of 3.71 shows +/– 5% error over the time series.

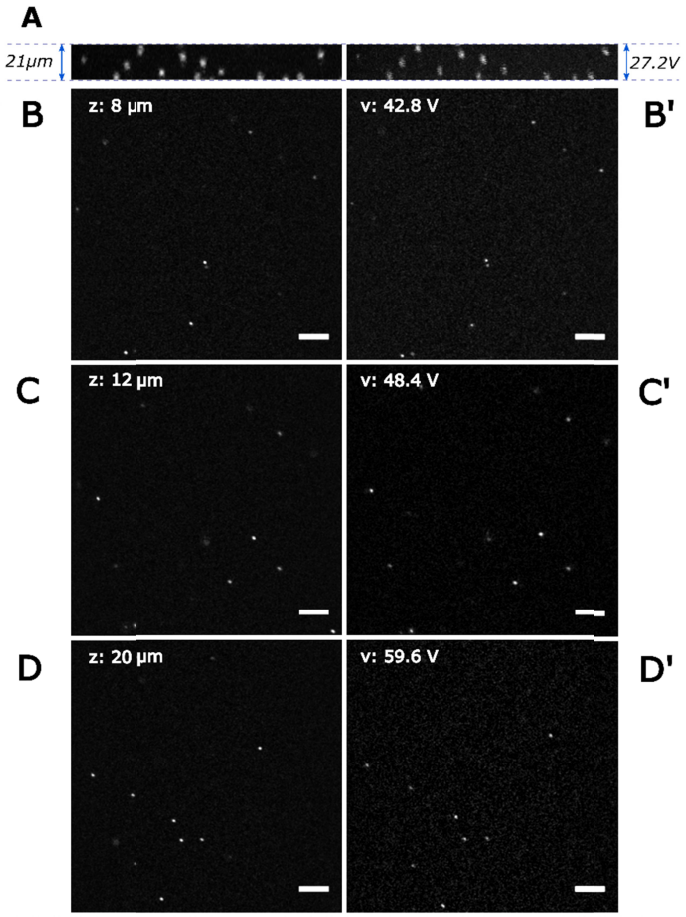

Fig. 4. - Calibration of axial scanning using 200 nm fluorescent microspheres in a polyacrylamide gel. Left panels: mechanical stage scanning. Right panels: Remote focusing using the liquid lens. (A) panels show axial sections (x-z), and (B)-(D) panels show lateral sections (x-y). The scalebar is 5 μm.

3.2. Liquid lens defocus calibration

We next calibrated the liquid lens defocus to the ground truth mechanical scanning method. For this purpose, we placed 200 nm beads in a thick gel, and imaged both with mechanical scanning and remote focusing (Fig. 4). Comparison between the axial sections (Fig. 4(a)) finds indistinguishable focusing between the two methods. We show different sections from the volume at different depth compared to their equivalent voltage (Fig. 4(b)-(d)). As expected from the wavefront measurements here we see a linear relationship between the mechanical scanning and remote focusing. We calculated a ratio of 1.4 V/μm for this configuration of the liquid lens remote focusing.

4. Results and discussion

We tested the liquid lens remote focusing on several live samples; here we present videos of 5D imaging of a single cell in suspension, mouse TA muscle mitochondrial function, bone blood flow in a mouse skull, and neural activity in the barrel cortex. All the volumetric images shown in this section are acquired with a triangle input waveform at a rate of 2.1 Hz,

Biomedical Optics EXPRESS

which translates to 4.2 volumes per second. With 110 frames per second imaging rate, 26 slices per volume were recorded.

The first example of our volumetric imaging is shown in Fig. 5. A single cell stained with DiD (697/58 nm emission filter and 775nm excitation) in suspension is shown moving filopodial extensions [32–34] around the cell, which is often associated with the first stages of cell adhesion to a surface and subsequent migration. The imaging volume is 42 µm x 42 µm x 28 µm (x,y,z) for this experiment.

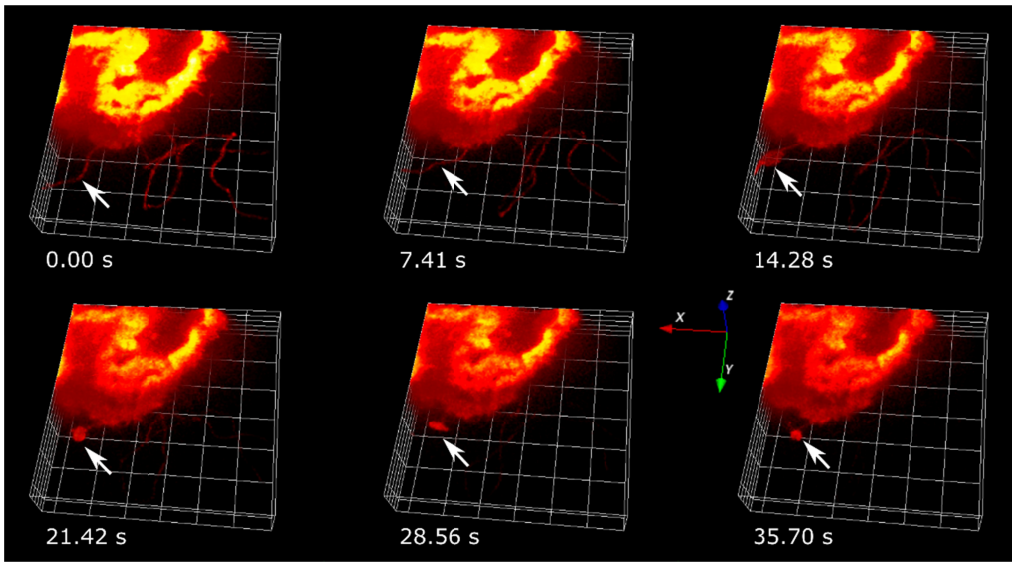

Fig. 5. - Volumetric imaging of a single cell in suspension. The MSC is isolated from a mouse and stained with DiD membrane dye. The field of view is 42 µm x 42 µm x 28 µm (x,y,z). 775 nm excitation light was used. Visualization 1 is available as supplementary.

The second sample imaged was the TA muscle with ubiquitous expression of Dendra2 in mitochondria (photo switchable fluorescent protein from green to red). To further look at dynamic electrical potential activity of the mitochondria we stained the muscle with TMRE [35] (mito-Dendra2 – green 509/22 nm filter, TMRE membrane potential dependent dye – red 585/40 nm filter, 775 nm excitation was used for simultaneous excitation of both), shown in Fig. 6(a). We observed fluctuations in the intensity of the fluorescence; some mitochondria (Fig. 6(b)) have increased potential in response to their environmental stimuli, such as adenosine triphosphate (ATP) production or generation of contractile force. This experiment demonstrated the potential of our liquid lens technology to monitor rapid mitochondrial responses to physiologically relevant stimuli. Volumetric imaging of the muscle sample enables study of mitochondrial activity at different depths simultaneously, which is important for future studies of muscle metabolism [36].

Biomedical Optics EXPRESS

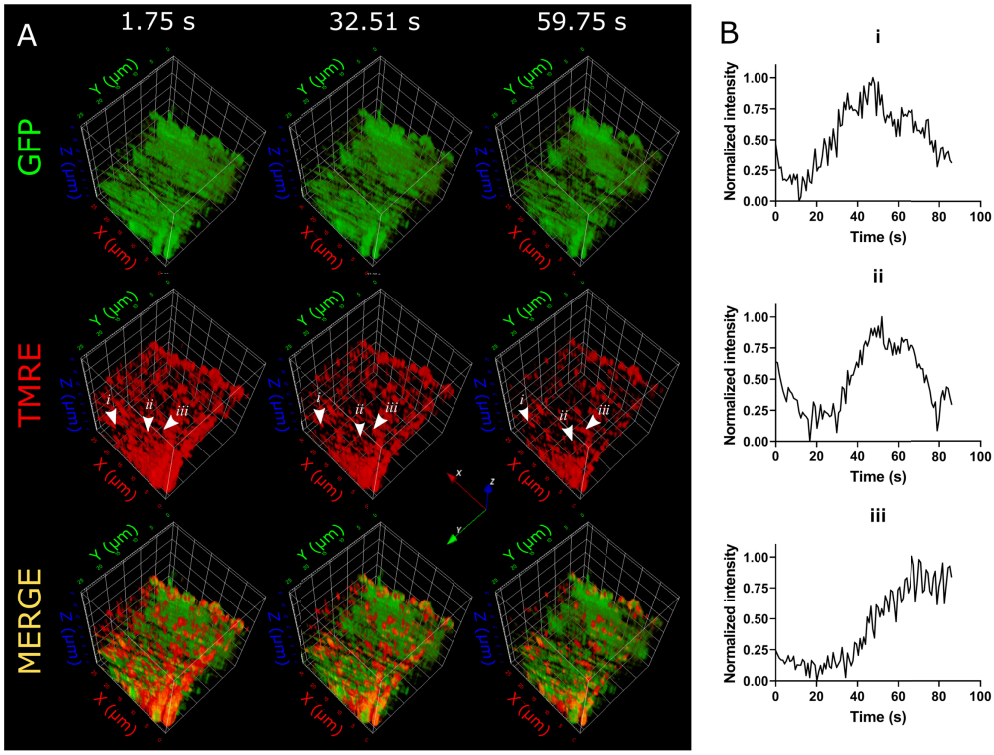

Fig. 6. - Multi-color volumetric imaging of a mouse TA muscle. In A green shows the ubiquitous expression of Dendra2 mitochondria, red is TMRE staining of mitochondria. The fluorescent fluctuations of mitochondria in A (i, ii, iii) are shown in B. The volume dimensions are 27 µm x 27 µm x 35 µm (x,y,z). 850 nm excitation light was used for imaging. Visualization 2 is available in the supplemental information.

Another dynamic *in vivo* sample that could benefit from volumetric imaging using a liquid lens is monitoring of the blood flow in the skull, which we also performed on a Dendra2 mitochondria mouse (Fig. 7). The blood flow is monitored by applying a rhodamine-B dextran conjugate to visualize the vasculature (585/40 nm filter, 840 nm excitation wavelength was used for both). Due to the lack of mitochondria in the red blood cells (RBC), they are seen as dark spots in the blood flow, however the GFP-labeled white blood cells (WBC) are visible moving through the vessels. Here we observed WBCs move at a rate of 10 µm/s, and RBCs travel at a rate of 20~300 µm/s. These velocities can vary dramatically depending on vessel diameter. Given our 4.2 Hz volumetric imaging speed over an area of 58 µm x 58 µm, in a small bone marrow vessel WBCs can easily be captured with good axial fidelity. However, given the axial sampling rate (26 frames per volume in this case), rapidly flowing RBCs exhibit an axial rolling shutter effect. In general, if we assume a criterion of having a particle travel 1/10 of the lateral field of view within one volume, given a field of view width of 58 µm used in this experiment, we can image particles that move at a rate of 24 µm/s. At travel rates higher than this, the volumes of the moving particles will be skewed in the direction of the travel. In such cases, technologies such as acousto-optics lens [11], or multi-plane imaging [5] could be beneficial, which require complicated synchronization, or computationally expensive reconstruction, respectively.

Biomedical Optics EXPRESS

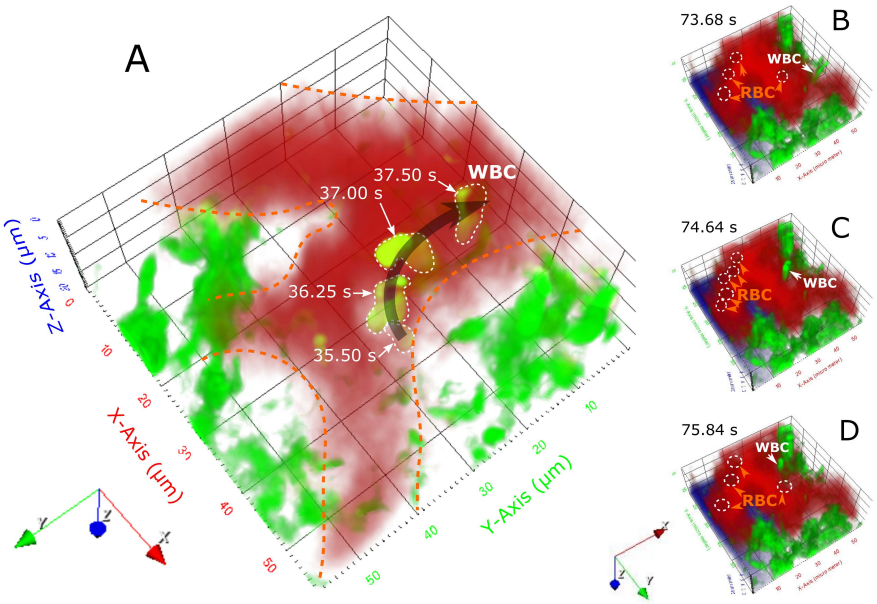

Fig. 7. - 3D visualization of blood flow in the skull of a mouse ubiquitously expressing Dendra2 (green) in mitochondria. Blue shows second harmonic generation of bone collagen fibers, and red shows Rhodamine B dextran conjugate present in the blood. Panel A shows an overview of a single WBC travelling in the vessel. B-D show different time points. The volume dimensions are 58 µm x 58 µm x 25 µm (x,y,z). Visualization 3 is available in the supplemental information.

Finally, we applied liquid lens volumetric imaging to brain activity in the barrel cortex of a mouse transfected with an R-GECO calcium indicator [37] (585/40 nm filter, and 1000 nm excitation light). To find the barrel cortex we imaged in one plane, and continuously stimulated by blowing puffs of air towards whiskers contralateral to the craniotomy site. Once activity was detected and a suitable location for imaging was found, we enabled the volumetric imaging procedure over an area of 80 µm x 80 µm x 25 µm (x,y,z). 4D (3D + time) registration was performed using ImageJ "Descriptor-based series registration (3d+t)" plugin [38]. For the automatic segmentation of the volume for active site analysis, we computed the average intensity over time for the whole volume from the registered volumetric series, applied intensity thresholding (Otsu Threshold), and morphological eroding (5 pixel radius sphere) and dilation (3 pixel radius sphere). Each area with connected elements were selected as separate regions of interest (ROI). These ROIs were then individually used to compute intensity fluctuations dF/F0, where F is the fluorescence intensity value, averaged over the volume at each time point of the time series, and a moving average F0 was used to obtain the calcium activity traces. The difference in ROI volumes is because the extent of the cells might be different or several cells within close vicinity of each other have been identified as one by the software. Figure 8 depicts the neural imaging, and its analysis. We observe neurons from different axial planes fire in response to air-blow stimulation of the whiskers (Fig. 8(c), neurons 3 and 4) in the contralateral side to the imaging site, and simultaneously identify neurons that do not respond to the whisker stimulus (Fig. 8©, neurons 1, 2, and 5) that may be involved in other processes.

Biomedical Optics EXPRESS

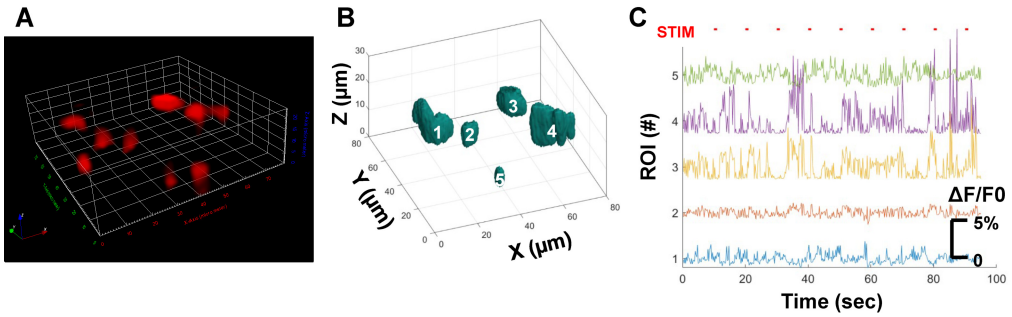

Fig. 8. Volumetric imaging of calcium activity in the mouse barrel cortex. (A) shows a pre-processed volumetric frame from the timelapse. The volume dimensions are 80 µm x 80 µm x 25 µm (x,y,z). After 3D registration several ROIs were located in the data set using mean volumetric fluorescence intensity, shown in (B). From each ROI, the intensity fluctuation is derived and background normalized (F0) to obtain the DF/F0 calcium activity fluctuations, shown in (C). The red ticks (STIM) indicate the timing of an air blow stimulation on the contralateral whiskers to the recording site. 1050 nm excitation light was used for imaging. Visualization 4 is available in the supplemental information.

5. Conclusions

In conclusion, we presented characterization and application of a liquid lens for fast volumetric imaging of in vivo samples. One main concern for using the liquid lens is the potential for optical aberrations due to the curvature produced by the electrical potential. Here we used a wavefront sensor for characterizing wavefront error produced by the liquid lens. We show that other than the desired defocus, astigmatism is the main aberration error in the system; which was minimized by fine alignment of the liquid lens, resulting in a minimal magnitude. Another major concern with using liquid lens technology for remote focusing of femtosecond pulsed lasers is the effect of high powered pulses on the performance and stability of the lens. We therefore measured the temperature of the body of the device and its hysteresis response after 2 hours of continuous exposure and did not observe a significant increase in the temperature, alteration of focusing speed, or alteration of focusing accuracy. We also measured the full range step response of the device and a settling response time of 92 ms. To speed up the axial scanning and avoid over/undershoots, we used a triangular waveform and an electrical low pass filter which eliminates the high frequency digitization effect. We then calibrated the remote focusing method versus a precise mechanical scanning method, and calculated the ratio of voltage to focal shift. And finally, we applied this method to several relevant in-vivo dynamically varying samples such as cells, muscle mitochondrial activity, intravital imaging of blood flow in the skull, and neural firing in the barrel cortex. Liquid lens technology has recently attracted attention for applications such as head-mountable brain neural activity measurement [39], or endoscopic imaging by providing both lateral [40] and axial [41,42] scanning. Due to their high potential for low cost and stability, many different methods of producing liquid lenses have been proposed. All of these methods and devices require careful characterization to generate high quality reproducible results. The characterization and calibration methods performed in this paper can be applied to those and other similar applications.

Funding

National Science Foundation (1706916); National Institutes of Health (R21EB027802); Center for Regenerative Engineering and Medicine (REM); Soft Bones Foundation.

Acknowledgments

We thank Varioptic for graciously providing the liquid lens for this research. We would like to thank Dr. Peter Kner for help with Shack-Hartmann wavefront sensors.

Biomedical Optics EXPRESS

Disclosures

The authors declare that there are no conflicts of interest related to this article.

References

1. W. Denk, J. H. Strickler, and W. W. Webb, "Two-photon laser scanning fluorescence microscopy," Science **248**(4951), 73–76 (1990).
2. W. R. Zipfel, R. M. Williams, and W. W. Webb, "Nonlinear magic: multiphoton microscopy in the biosciences," Nat. Biotechnol. **21**(11), 1369–1377 (2003).
3. T. A. Pologruto, B. L. Sabatini, and K. Svoboda, "ScanImage: flexible software for operating laser scanning microscopes," Biomed. Eng. Online **2**(1), 13 (2003).
4. Z. Kam, P. Kner, D. Agard, and J. W. Sedat, "Modelling the application of adaptive optics to wide-field microscope live imaging," J. Microsc. **226**(1), 33–42 (2007).
5. M. A. Taylor, T. Nöbauer, A. Pernia-Andrade, F. Schlumm, and A. Vaziri, "Brain-wide 3D light-field imaging of neuronal activity with speckle-enhanced resolution," Optica **5**(4), 345–353 (2018).
6. W. Yang, J. E. Miller, L. Carrillo-Reid, E. Pnevmatikakis, L. Paninski, R. Yuste, and D. S. Peterka, "Simultaneous Multi-plane Imaging of Neural Circuits," Neuron **89**(2), 269–284 (2016).
7. A. Cheng, J. T. Gonçalves, P. Golshani, K. Arisaka, and C. Portera-Cailliau, "Simultaneous two-photon calcium imaging at different depths with spatiotemporal multiplexing," Nat. Methods **8**(2), 139–142 (2011).
8. S. Abrahamsson, H. Blom, A. Agostinho, D. C. Jans, A. Jost, M. Müller, L. Nilsson, K. Bernhem, T. J. Lambert, R. Heintzmann, and H. Brismar, "Multifocus structured illumination microscopy for fast volumetric super-resolution imaging," Biomed. Opt. Express **8**(9), 4135–4140 (2017).
9. R. Attota, "Through-focus or volumetric type of optical imaging methods: a review," in (SPIE, 2018), 10.
10. P. Rupprecht, A. Prendergast, C. Wyart, and R. W. Friedrich, "Remote z-scanning with a macroscopic voice coil motor for fast 3D multiphoton laser scanning microscopy," Biomed. Opt. Express **7**(5), 1656–1671 (2016).
11. P. A. Kirkby, K. M. N. Srinivas Nadella, and R. A. Silver, "A compact acousto-optic lens for 2D and 3D femtosecond based 2-photon microscopy," Opt. Express **18**(13), 13720–13745 (2010).
12. L. Kong, J. Tang, J. P. Little, Y. Yu, T. Lämmermann, C. P. Lin, R. N. Germain, and M. Cui, "Continuous volumetric imaging via an optical phase-locked ultrasound lens," Nat. Methods **12**(8), 759–762 (2015).
13. M. Žurauskas, O. Barnstedt, M. Frade-Rodriguez, S. Waddell, and M. J. Booth, "Rapid adaptive remote focusing microscope for sensing of volumetric neural activity," Biomed. Opt. Express **8**(10), 4369–4379 (2017).
14. W. J. Shain, N. A. Vickers, B. B. Goldberg, T. Bifano, and J. Mertz, "Extended depth-of-field microscopy with a high-speed deformable mirror," Opt. Lett. **42**(5), 995–998 (2017).
15. K. Dobek, "Motionless microscopy with tunable thermal lens," Opt. Express **26**(4), 3892–3902 (2018).
16. M. Bawart, A. Jesacher, and M. Ritsh-Marte, "Remote focusing in confocal microscopy by means of a modified Alvarez lens," J. Microsc. **271**(3), 337–344 (2018).
17. B. Berge and J. Peseux, "Variable focal lens controlled by an external voltage: An application of electrowetting," Eur. Phys. J. E **3**(2), 159–163 (2000).
18. B. H. W. Hendriks, S. Kuiper, M. A. J. Van As, C. A. Renders, and T. W. Tukker, "Electrowetting-Based Variable-Focus Lens for Miniature Systems," Opt. Rev. **12**(3), 255–259 (2005).
19. M. Sato, Y. Motegi, S. Yagi, K. Gengyo-Ando, M. Ohkura, and J. Nakai, "Fast varifocal two-photon microendoscope for imaging neuronal activity in the deep brain," Biomed. Opt. Express **8**(9), 4049–4060 (2017).
20. D. Trung-Dung, P. Cheol-Woo, and K. Gyu-Man, "Fabrication of Focus-Variable Fluidic Microlens Using Single Casting," Jpn. J. Appl. Phys. **50**(6S), 06GM15 (2011).
21. R. Marks, D. L. Mathine, J. Schwiegerling, G. Peyman, and N. Peyghambarian, "Astigmatism and defocus wavefront correction via Zernike modes produced with fluidic lenses," Appl. Opt. **48**(19), 3580–3587 (2009).
22. Z. Ding, C. Wang, Z. Hu, Z. Cao, Z. Zhou, X. Chen, H. Chen, and W. Qiao, "Surface profiling of an aspherical liquid lens with a varied thickness membrane," Opt. Express **25**(4), 3122–3132 (2017).
23. B. F. Grewe, F. F. Voigt, M. van 't Hoff, and F. Helmchen, "Fast two-layer two-photon imaging of neuronal cell populations using an electrically tunable lens," Biomed. Opt. Express **2**(7), 2035–2046 (2011).
24. F. O. Fahrbach, F. F. Voigt, B. Schmid, F. Helmchen, and J. Huisken, "Rapid 3D light-sheet microscopy with a tunable lens," Opt. Express **21**(18), 21010–21026 (2013).
25. J. David Giese, T. N. Ford, and J. Mertz, "Fast volumetric phase-gradient imaging in thick samples," Opt. Express **22**(1), 1152–1162 (2014).
26. A. H. Pham, J. M. McCaffery, and D. C. Chan, "Mouse lines with photo-activatable mitochondria to study mitochondrial dynamics," Genesis **50**(11), 833–843 (2012).
27. H. Dana, B. Mohar, Y. Sun, S. Narayan, A. Gordus, J. P. Hasseman, G. Tsegaye, G. T. Holt, A. Hu, D. Walpita, R. Patel, J. J. Macklin, C. I. Bargmann, M. B. Ahrens, E. R. Schreiter, V. Jayaraman, L. L. Looger, K. Svoboda, and D. S. Kim, "Sensitive red protein calcium indicators for imaging neural activity," eLife **5**, e12727 (2016).
28. L. A. Poyneer, D. T. Gavel, and J. M. Brase, "Fast wave-front reconstruction in large adaptive optics systems with use of the Fourier transform," J. Opt. Soc. Am. A **19**(10), 2100–2111 (2002).
29. R. J. Noll, "Zernike polynomials and atmospheric turbulence," J. Opt. Soc. Am. **66**(3), 207–211 (1976).
30. D. C. Giancoli, *Physics for Scientists and Engineers with Modern Physics,* Volume 1, Fourth ed. (Pearson Education, 2008).
31. K. Ogata, *System Dynamics*, Fourth ed. (Pearson/Prentice Hall, 2004).

Biomedical Optics EXPRESS

32. G. S. L. Teo, J. A. Ankrum, R. Martinelli, S. E. Boetto, K. Simms, T. E. Sciuto, A. M. Dvorak, J. M. Karp, and C. V. Carman, "Mesenchymal stem cells transmigrate between and directly through tumor necrosis factor-α-activated endothelial cells via both leukocyte-like and novel mechanisms," Stem Cells **30**(11), 2472–2486 (2012).
33. M.-C. Kim, Y. R. Silberberg, R. Abeyaratne, R. D. Kamm, and H. H. Asada, "Computational modeling of three-dimensional ECM-rigidity sensing to guide directed cell migration," Proc. Natl. Acad. Sci. U.S.A. **115**(3), E390–E399 (2018).
34. M.-C. Kim, J. Whisler, Y. R. Silberberg, R. D. Kamm, and H. H. Asada, "Cell Invasion Dynamics into a Three Dimensional Extracellular Matrix Fibre Network," PLOS Comput. Biol. **11**(10), e1004535 (2015).
35. K. F. Tehrani, E. G. Pendleton, W. M. Southern, J. A. Call, and L. J. Mortensen, "Two-photon deep-tissue spatially resolved mitochondrial imaging using membrane potential fluorescence fluctuations," Biomed. Opt. Express **9**(1), 254–259 (2018).
36. W. M. Southern, A. S. Nichenko, K. F. Tehrani, M. J. McGranahan, L. Krishnan, A. E. Qualls, N. J. Jenkins, L. J. Mortensen, H. Yin, A. Yin, R. E. Guldberg, S. M. Greising, and J. A. Call, "PGC-1α overexpression partially rescues impaired oxidative and contractile pathophysiology following volumetric muscle loss injury," bioRxiv **9**(1), 535328 (2019).
37. Y. Zhao, S. Araki, J. Wu, T. Teramoto, Y.-F. Chang, M. Nakano, A. S. Abdelfattah, M. Fujiwara, T. Ishihara, T. Nagai, and R. E. Campbell, "An expanded palette of genetically encoded Ca^{2+} indicators," Science **333**(6051), 1888–1891 (2011).
38. S. Preibisch, S. Saalfeld, J. Schindelin, and P. Tomancak, "Software for bead-based registration of selective plane illumination microscopy data," Nat. Methods **7**(6), 418–419 (2010).
39. B. N. Ozbay, G. L. Futia, M. Ma, V. M. Bright, J. T. Gopinath, E. G. Hughes, D. Restrepo, and E. A. Gibson, "Three dimensional two-photon brain imaging in freely moving mice using a miniature fiber coupled microscope with active axial-scanning," Sci. Rep. **8**(1), 8108 (2018).
40. O. D. Supekar, B. N. Ozbay, M. Zohrabi, P. D. Nystrom, G. L. Futia, D. Restrepo, E. A. Gibson, J. T. Gopinath, and V. M. Bright, "Two-photon laser scanning microscopy with electrowetting-based prism scanning," Biomed. Opt. Express **8**(12), 5412–5426 (2017).
41. H.-S. Chen and Y.-H. Lin, "An endoscopic system adopting a liquid crystal lens with an electrically tunable depth-of-field," Opt. Express **21**(15), 18079–18088 (2013).
42. Y. Zou, W. Zhang, F. S. Chau, and G. Zhou, "Miniature adjustable-focus endoscope with a solid electrically tunable lens," Opt. Express **23**(16), 20582–20592 (2015).